








Controlling interlayer excitons in MoS₂ layers grown by chemical vapor deposition

Ioannis Paradisanos^{1,6}, Shivangi Shree^{1,6}, Antony George ², Nadine Leisgang ³, Cedric Robert¹, Kenji Watanabe ⁴, Takashi Taniguchi⁴, Richard J. Warburton ³, Andrey Turchanin^{2,5}, Xavier Marie ¹, Iann C. Gerber ¹✉ & Bernhard Urbaszek ¹✉

Combining MoS₂ monolayers to form multilayers allows to access new functionalities. Deterministic assembly of large area van der Waals structures requires concrete indicators of successful interlayer coupling in bilayers grown by chemical vapor deposition. In this work, we examine the correlation between the stacking order and the interlayer coupling of valence states in both as-grown MoS₂ homobilayer samples and in artificially stacked bilayers from monolayers, all grown by chemical vapor deposition. We show that hole delocalization over the bilayer is only allowed in 2H stacking and results in strong interlayer exciton absorption and also in a larger A-B exciton separation as compared to 3R bilayers. Comparing 2H and 3R reflectivity spectra allows to extract an interlayer coupling energy of about $t_{\perp} = 49$ meV. Beyond DFT calculations including excitonic effects confirm signatures of efficient interlayer coupling for 2H stacking in agreement with our experiments.

¹Université de Toulouse, INSA-CNRS-UPS, LPCNO, 135 Avenue Rangueil, 31077 Toulouse, France. ²Institute of Physical Chemistry, Friedrich Schiller University Jena, 07743 Jena, Germany. ³Department of Physics, University of Basel, Basel, Switzerland. ⁴National Institute for Materials Science, Tsukuba 305-0044 Ibaraki, Japan. ⁵Abbe Centre of Photonics, 07745 Jena, Germany. ⁶These authors contributed equally: Ioannis Paradisanos, Shivangi Shree. ✉email: igerber@insa-toulouse.fr; urbaszek@insa-toulouse.fr

Transition metal dichalcogenides (TMDs) with the form MX_2 ($M = \text{Mo}, \text{W}, \text{Ti}, \text{etc.}$ and $X = \text{S}, \text{Se}, \text{Te}$) have tunable electronic properties from metallic to semiconducting depending on the crystal symmetry, composition, and number of layers^{1–9}. The band structure of TMD semiconductors is drastically modified by changing the sample thickness by just one atomic monolayer^{10–12}. For instance, the combination of two different monolayer materials such as MoSe_2 – WSe_2 into a heterobilayer results in type II band alignment and opens new research perspectives on periodic moiré potentials for carriers in the different layers and the resulting interlayer excitons^{13–17}. Twisted homobilayers of graphene, WSe_2 , and MoSe_2 allow accessing new superconducting phases and correlated insulating states^{18–20}. To access the new functionalities provided by assembling monolayers to form multilayers it is necessary to identify physical parameters that strongly depend on interlayer coupling and to experimentally control them. One approach is to compare chemical vapor deposition (CVD)-grown MoS_2 bilayers with artificially stacked bilayers made from CVD monolayers with 2H (180° twist angle) and 3R (0° twist angle) stacking. Studying these two precise alignments is also relevant for samples initially assembled with other twist angles as reconstruction results also in these experiments in the formation of μm -wide 2H and 3R areas^{21,22}, which are energetically most stable. To artificially stack large area CVD layers and control interlayer coupling through stacking (i.e., 0° or 180° twist angle) is technologically relevant for 2D materials optoelectronics¹⁷, as CVD substrates are covered by a large number of monolayers and are very practical to stack (twist) due to their symmetric triangular shape and well-characterized edge termination.

Here we show that the valence states for 2H bilayers are strongly impacted by interlayer coupling as the hole is delocalized over the two layers^{23–25}. This results in important changes in the optical spectra governed by K–K transitions as we observe strong absorption from interlayer excitons and a clear change in separation between A- to B-exciton transition in differential white light reflection at $T = 4 \text{ K}$. These observations are made possible due to the drastically improved optical quality of CVD samples removed from the growth substrate and encapsulated in hBN²⁶. We show that both indicators for interlayer coupling are absent in

the measured 3R bilayer spectra as a hole hopping between the layers is symmetry forbidden²⁷. Comparing for 3R (no interlayer coupling) and for 2H the A–B exciton absorption spectra allows us to extract an experimental value of the perpendicular hopping (coupling) term of $t_\perp \approx 49 \text{ meV}$, important for moiré superlattices²⁸ and so far only roughly estimated from theory²⁷.

In addition to our optical spectroscopy experiments we show in density functional theory (DFT) calculations, as well as by applying GW-type approaches, that the valence band (VB) splittings for 2H as compared to 3R are different due to interlayer coupling. In our calculated absorption spectra, including excitonic effects by solving the Bethe–Salpeter-equation (BSE) on top of GW calculations, for 2H stacking we show strong interlayer exciton absorption, absent for 3R stacking.

Results

Interlayer excitons in as-grown CVD MoS_2 homobilayers. The thermodynamically most stable configurations of TMD homobilayers are the 2H and the 3R stacking^{24,30}. In practice, most naturally occurring molybdenite shows 2H, not 3R stacking. In this work, we focus on high-quality CVD-grown flakes for several reasons: during CVD growth of MoS_2 both 2H and 3R stackings for bilayers can occur³¹ and we are therefore able to compare the optical response for samples grown under identical conditions. Secondly, as all CVD flakes on our substrate show the same edge termination, we can artificially stack two layers in 2H and 3R configuration with a precise twist angle to compare with the as-grown samples—see “Discussion” below. Third, many monolayers cover the SiO_2 substrate and can all be picked up in a single step, which makes fabrication of bilayer structures very efficient. CVD flakes with a larger surface area are also more convenient to fabricate devices with electrical contacts.

Optical microscope images of as-grown CVD bilayers on SiO_2/Si with 3R and 2H stacking are presented in Fig. 1a. The stacking can be determined already by the relative rotation of the triangular monolayers and is confirmed in second harmonic generation (SHG) experiments^{33,34}. The SHG signal for 2H stacking was not detectable (inversion symmetry restored) but we could perform detailed angle-dependent SHG for the 3R stacking

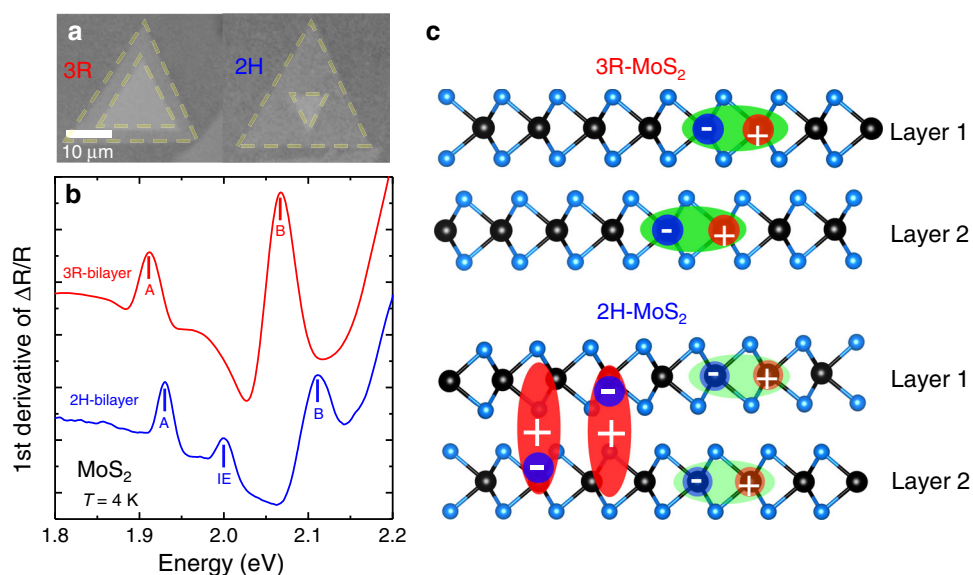


Fig. 1 Spectroscopy of as-grown CVD bilayers encapsulated in hBN. **a** Optical microscope images of as-grown 3R (left) and 2H CVD MoS_2 bilayers (right) on SiO_2/Si before pick-up. **b** First derivative of white light reflection spectrum for as-grown 2H-bilayer (blue) and as-grown 3R-bilayer (red), recorded at $T = 4 \text{ K}$, both bilayers are encapsulated in high-quality hBN for optical spectroscopy²⁹. **c** Schematic of 3R stacked bilayer with intralayer excitons (top) compared to 2H stacked bilayer where in addition interlayer excitons are observed as in panel (b).

(broken inversion symmetry), see Supplementary Figs. 1 and 2. The high-quality MoS₂ bilayers and monolayers were grown by a modified CVD process in which a Knudsen-type effusion cell is used for the delivery of sulfur precursor³⁵. Using a water-assisted pick-up technique³², the as-grown CVD bilayers have been deterministically transferred and encapsulated in hBN to achieve high optical quality²⁶, which has recently been shown to be crucial for optical spectroscopy on CVD samples lowering the typical emission linewidth from about 50 meV to below 5 meV at $T = 4$ K. An example of a photoluminescence spectrum of a CVD MoS₂ monolayer used here is shown in Supplementary Fig. 3. The thickness of the top and bottom hBN has been carefully selected to optimize the oscillator strength of the interlayer excitons (IEs)²⁴. After encapsulation, the samples were cooled down to $T = 4$ K in a closed-cycle cryostat and a series of differential reflectivity measurements with a home-built confocal microscope have been performed at different locations of the samples, see “Methods”. We define differential reflectivity as $(R_{\text{sam}} - R_{\text{sub}})/R_{\text{sub}}$, where R_{sam} is the intensity reflection coefficient of the sample with the MoS₂ layers and R_{sub} is the same structure without the MoS₂. Note that the overall shape and amplitude of the differential reflectivity signal also depends on cavity effects (thin-layer interference) given by top and bottom hBN and SiO₂ layer thickness (see ref. ³⁶ for details). In Fig. 1b, the first derivative of the differential reflectivity spectra for as-grown CVD 2H and 3R MoS₂ bilayers can be compared, see Supplementary Fig. 5 for differential reflection spectra. There are two striking differences between the 2H and 3R bilayer spectra: (i) While A and B intralayer excitons are identified for both configurations, a pronounced feature at ≈ 2 eV appears exclusively in the 2H bilayer. This feature is assigned to an interlayer state, its energy being in good agreement with the very recently identified IEs in high quality and hBN encapsulated, exfoliated MoS₂ bilayers with 2H stacking^{23,24,37}, in contrast to CVD-grown samples studied here. This observation of IEs is made possible by our specific CVD sample preparation for the optical spectroscopy experiment²⁶. IE absorption was not detectable in very detailed earlier works due to considerably larger optical linewidth or detection of emission and not absorption^{38–41}. In contrast to 2H stacking, in the 3R configuration no additional states are detected between the A- and B-excitons, thus indicating that the delocalization of holes is not allowed in this particular stacking order²⁴, see below for a more detailed discussion. (ii) The separation between the A- and B-exciton transitions is considerably larger in the 2H bilayers (about 185 meV) as compared to the 3R bilayer (about 150 meV, mainly given by the spin-orbit splitting in the VBs). This is a second indication for efficient interlayer coupling of A–B valence states for 2H stacking, as the separation of the valence states mainly governs the A–B exciton separation^{23,27,42}.

Controlling interlayer coupling through stacking. In Fig. 1 we show that as-grown CVD MoS₂ bilayers experience interlayer coupling resulting in interlayer exciton formation, here observed for a non-contaminated interface between the top and bottom layer. Contamination from secondary transfer processes could potentially suppress the coupling between the layers and hence IE formation. By choosing 2H or 3R orientation manually when stacking CVD-grown monolayers to form bilayers one can allow or disallow hole tunneling between the layers, respectively. This requires to pick-up the CVD-grown monolayers from their growth substrate while maintaining their structural integrity, optical quality, and a sufficiently clean interface after transfer. Furthermore, fine control of the twist angle between the top and bottom layer is needed, since the IE formation is allowed only in a precise stacking order, see sample preparation schematic in

Fig. 2a. Here we use water-assisted deterministic transfer that allows the ability to controllably assemble CVD bilayers with the desired twist angle³². First, CVD-grown monolayers have been carefully picked up from the growth substrate and transferred to polydimethylsiloxane (PDMS) (Fig. 2b)^{32,43}. The structural integrity of the CVD-grown monolayers is preserved in this case and the following step is to slowly assemble 2H and 3R bilayers and encapsulate them in hBN as shown in Fig. 2c. Small deviations from 0° or 180° twist angle are expected but natural reconstruction of the bilayer will again favor the lowest energy arrangement, 3R and 2H, respectively^{21,22}.

Differential reflectivity spectra have been collected from 10 different areas of the assembled 2H and 3R bilayers of Fig. 2c. In Fig. 2d, three typical examples of the assembled 2H and 3R spectra are presented. The spectra show a striking resemblance with the as-grown bilayer spectra discussed before in Fig. 1b. So also for the assembled 2H bilayers we identify clear interlayer exciton absorption and an increased separation between the A- and B-excitons. It is important to note that the IE transition was clearly observed over the whole surface area of the manually constructed 2H bilayer. We take it as a strong indication of efficient interlayer coupling and possibly efficient reconstruction/self-rotation to the 2H configuration. We therefore further confirm the formation of IEs exclusively in the 2H stacking. By manually choosing the stacking configuration i.e., twist angle, it is possible to tune the VB splitting and the formation of interlayer excitons in a large area, high-quality CVD samples.

Beyond-DFT band structure calculations including GW+BSE.

In addition to optical spectroscopy we perform beyond DFT calculations to study the striking differences between 2H and 3R MoS₂ bilayers, see “Methods” for the computational details. Please note that our GW+BSE calculations are performed for MoS₂ bilayers in vacuum for simplicity and not in hBN. The general target of our calculations is to understand the microscopic origin of the optical transitions and to reproduce the energetic order qualitatively. In GW calculations we compare band structures corrected by screening effects, the exciton description being added later. In the vicinity of the K-point of the Brillouin zone, see Fig. 3a and schematic in Fig. 3c, differences between 2H and 3R stacking in VB and VB₋₁ states are clear. We find a VB splitting in the 2H bilayer that is 19 meV larger than in the 3R bilayer. By solving the BSE we obtain the absorption for the 2H and 3R bilayers shown in Fig. 3b. The main characteristics are (i) the presence of a strong interlayer exciton peak in 2H and (ii) a larger A–B exciton separation for 2H than for 3R configuration, exactly as found in the experiments in Figs. 1 and 2. Interestingly, in 3R stacking, there is a minor departure from degeneracy that splits VB and VB₋₁ states from distinct layers when they remain degenerate in 2H configuration. As a consequence, two distinct A-type excitons separated by only 14 meV constitute the A-peak of the 3R-bilayer absorption spectrum in our calculation, explaining its larger width compared to the 2H case, see Fig. 3c. The origin of this splitting, that keeps VB(L1) and VB(L2) states to be of the same spin-states, is the lack of symmetry inversion combined with different atomic environments for Mo atoms⁴⁴. This is especially true for the VBs since the atomic orbitals that constitute those states are particularly sensitive to crystal field splitting.

Discussion

To summarize the main experimental findings, first we observe strong interlayer exciton absorption between the main A- and B-exciton transitions for CVD-grown (Fig. 1b) and artificially stacked (Fig. 2d) 2H bilayers, whereas this interlayer transition is

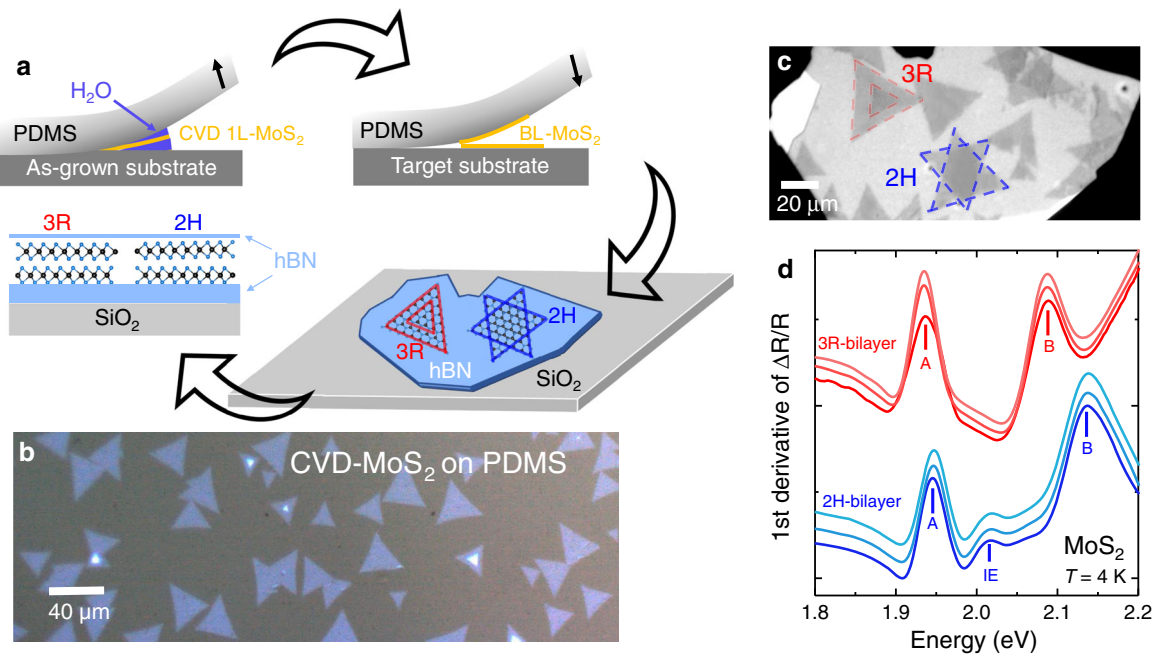


Fig. 2 Artificial stacking of CVD monolayers into bilayers. **a** Schematic of sample pick-up, bilayer assembly, and encapsulation for optics. **b** Optical micrograph of CVD-grown MoS₂ monolayers and a few homobilayers, transferred to the PDMS stamp following water-assisted pick-up³² from the growth substrate. **c** Artificially-assembled 3R and 2H MoS₂ homobilayers, fabricated by an all-dry deterministic transfer process. **d** First derivative of reflectivity spectra collected from three different areas of the artificially stacked 3R (red) and 2H (blue) MoS₂ homobilayers, shown in (c). Spectra have been shifted for clarity.

absent for 3R stacking as hole tunneling is symmetry forbidden and only intralayer exciton transitions are observed. A second striking observation is that the stacking of the layers also affects the energy difference between A- and B-exciton transitions. This is demonstrated in Fig. 3d, where the A–B exciton energy difference is compared between as-grown and assembled 2H and 3R bilayers. It is apparent that 2H bilayers exhibit a significantly larger energy difference between the A- and B-exciton states, compared to 3R bilayers.

Our next target is to experimentally extract the interlayer hopping term, t_{\perp} based on a k - p model of bilayers in the vicinity of K points^{23,27,28} and compare it to post-DFT estimates. As indicated in Fig. 3c, for 3R stacking the measured A- to B-exciton splitting S_{3R} is roughly given by the spin-orbit splitting as $S_{3R} = \Delta_{SO}$. For 2H-stacking the A–B splitting in the valence band depends on the coupling energy t_{\perp} as $S_{2H} = \sqrt{\Delta_{SO}^2 + 4t_{\perp}^2}$ and hence

$$t_{\perp} = \sqrt{\frac{S_{2H}^2 - \Delta_{SO}^2}{4}}, \quad (1)$$

where S_{2H} is the measured A–B exciton splitting of the as-grown 2H MoS₂ bilayer and as a value for Δ_{SO} we take the measured A–B separation in the 3R sample. For $S_{2H} = 183$ meV and $\Delta_{SO} = 155$ meV, we obtain $t_{\perp} \approx 49$ meV. This value can be compared to the ones extracted from our standard DFT calculations as previously done²⁷, or from more advanced GW and GW+BSE calculations. Table 1 summarizes calculated valence band splittings and A–B energy differences for monolayer, 2H and 3R stacking as well as the corresponding coupling strength, directly extracted from the VB splitting as in ref. 28 or Eq. (1). The agreement between theoretical, including previous rough estimates²⁷, and experimental results is good as we reproduce the larger A–B splitting for the 2H bilayers as compared to 3R. Although we measure exciton transitions and not directly the VB splitting in

the 2H bilayer, the agreement between theory and experiment strongly supports our interpretation for the reason behind the different A–B exciton splitting. It should be noted that for 3R bilayers, $t_{\perp} = 0$ since interlayer hopping is not allowed in this case. This short numerical analysis highlights that the efficiency of this interlayer coupling will depend on the ratio of t_{\perp} versus the spin-orbit VB splitting⁴⁵, which is much smaller in MoS₂ ($\Delta_{SO} \approx 150$ meV) as compared to WSe₂ ($\Delta_{SO} \approx 430$ meV). This leads in principle to tunable interlayer coupling for MoS₂⁴⁶ and so-called spin-layer-locking for WSe₂ bilayers⁴⁷.

Larger A–B exciton splitting in bulk MoS₂ for 2H compared to 3R stacking has also been demonstrated in early experiments using optical transmission spectroscopy^{48,49} and more recently in angle-resolved electron emission spectroscopy⁵⁰. The A–B exciton splitting in MoS₂ bilayers has been previously studied by several groups^{38,51–54}. In these reports, the spin-orbit coupling and interlayer coupling have been discussed, but neither interlayer exciton formation nor an experimental analysis of the coupling term t_{\perp} . In our study, the direct comparison in the same set-up on the same substrate of 2H and 3R bilayers with good optical quality due to encapsulation allows to determine the difference in A–B exciton energies precisely, which we ascribe to interlayer coupling, as supported by our quasi-particle GW and absorption spectrum including excitonic effects calculations. From an experimental point of view, our results suggest two practical test criteria for interlayer coupling following artificial stacking: the strong interlayer exciton absorption and the clear difference in A–B exciton transition energies. The physics discussed here for 2H and 3R bilayers is also relevant for samples with a twist angle slightly different from 0° or 180° as reconstruction/self-rotation results in artificial stacks typically in large areas of 2H and 3R stacking, which will show the optical properties of the samples investigated here. Interestingly, interlayer exciton absorption has been reported in bulk 2H-MoTe₂ and bulk 2H-MoSe₂^{55,56}. Please see ref. 57 for related work on bilayer MoS₂.

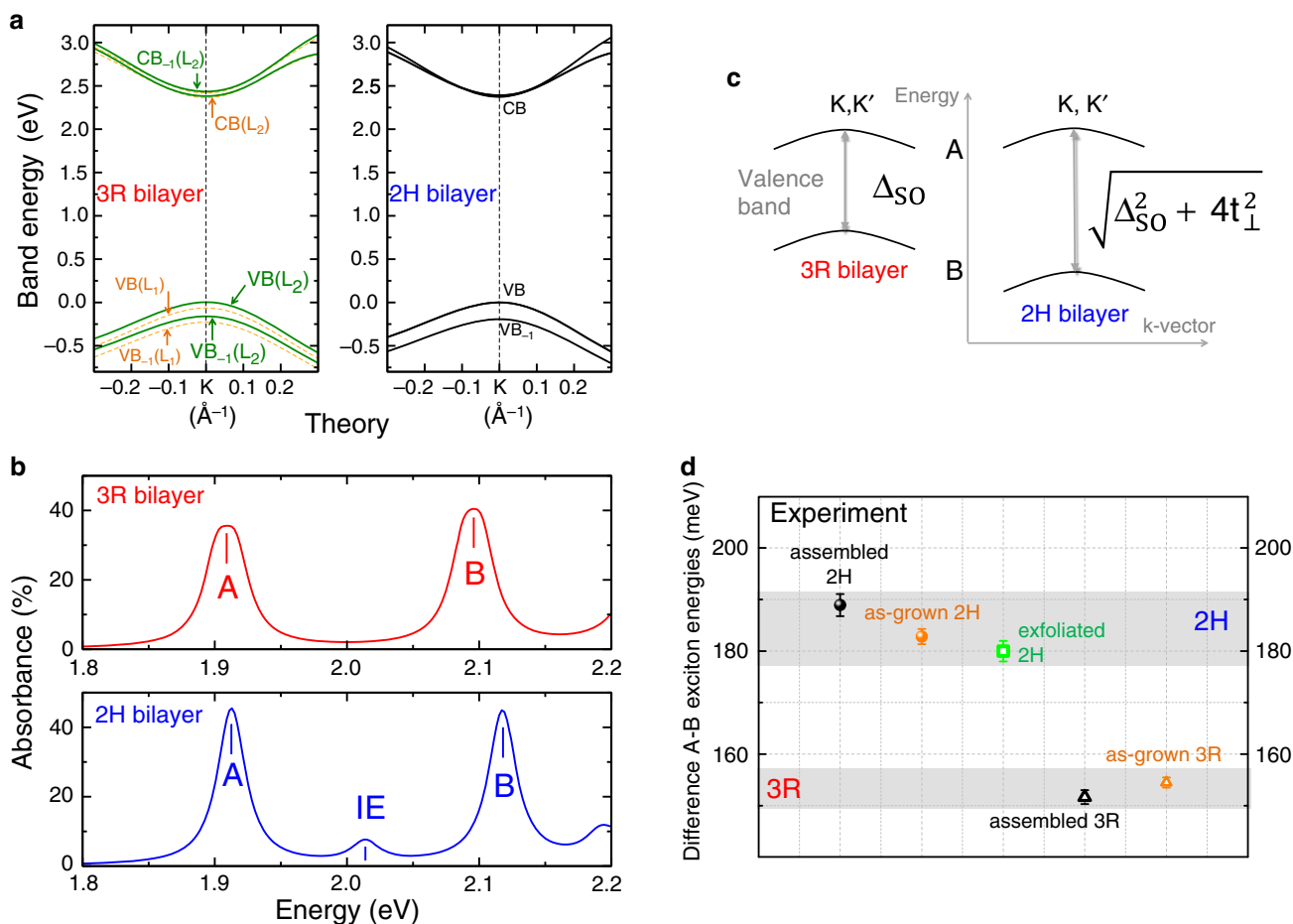


Fig. 3 Interlayer coupling in theory and experiment. **a** Valence and conduction bands around K-point calculated at the G_0W_0 level for 2H and 3R stacking, with the energy value of the VB set to 0 in K. **b** Calculated absorption using G_0W_0 +BSE approach for both stackings, see “Methods” for the computational details. Complete band structures are given in Supplementary Fig. 4. **c** Schematic of the A- and B-valence bands for 3R bilayers (left) and 2H bilayers (right) as a function of the spin-orbit splitting Δ_{SO} and the interlayer coupling parameter t_{\perp} . **d** Energy difference between B- and A-exciton for the as-grown (orange), as well as artificially-assembled (black) 2H and 3R MoS₂ homobilayers. The error bars represent the standard deviation extracted over 10 different spectra in each case. Gray shaded area is a guide to the eye to underline clear differences between 3R and 2H bilayers.

Table 1 Valence band splittings, A-B transition energy differences (S) extracted from GW and GW+BSE calculations and the corresponding interlayer coupling parameters.

	Monolayer	3R-bilayer	2H-bilayer	t_{\perp}
VB splitting	178 (189)	175 (189)	194 (203)	57 (42)
S	185	186	205	43

Values extracted for standard DFT calculations are in parentheses. All values are given in meV.

Methods

CVD samples growth. MoS₂ crystals were grown on thermally oxidized silicon substrates (Siltronix, oxide thickness 300 nm, roughness <0.2 nm RMS) by a modified CVD growth method in which a Knudsen-type effusion cell is used for the delivery of sulfur precursor³⁵.

Sample pick-up and encapsulation. The SiO₂/Si substrate for hosting the van der Waals structure was cleaned with a 10-min ultrasonication bath in acetone and isopropanol followed by oxygen plasma exposure. A clean PDMS stamp was first placed on a glass slide and the SiO₂/Si substrate containing the as-grown CVD MoS₂ monolayers and homobilayers was brought in contact with the PDMS stamp³². The substrate was pressed against the PDMS stamp and distilled water droplets were injected at the perimeter of the substrate. Water droplets penetrated

into the SiO₂/MoS₂/PDMS interface and after 1 min the SiO₂/Si substrate was carefully lifted, resulting into the transfer of a large area of CVD-grown MoS₂ triangles onto the PDMS stamp, as shown in Fig. 2b. During the water-assisted pick-up technique, high-purity (>20 MΩ) deionized water was used and the samples were dried with a nitrogen gun. Finally, hBN flakes were exfoliated from high-quality bulk crystal²⁹ onto the target substrate and subsequent deterministic-dry transfer of the CVD-grown MoS₂ triangles from the PDMS stamp on top of the hBN was applied. Thermal annealing at 150° for 30 min is performed after each transfer step.

Optical spectroscopy set-up. Low-temperature reflectance measurements were performed in a home-built micro-spectroscopy set-up assembled around a closed-cycle, low vibration attoDry cryostat with a temperature controller ($T = 4-300$ K). The white light source for reflectivity is a halogen lamp with a stabilized power supply focussed initially on a pin-hole that is imaged on the sample. The emitted and/or reflected light is dispersed in a spectrometer and detected by a Si-CCD camera. The excitation/detection spot diameter is $\approx 1 \mu\text{m}$, i.e., smaller than the typical size of the homobilayers.

Methods for DFT and GW calculations. The atomic structures, the quasi-particle band structures, and optical spectra have been obtained from DFT calculations using the VASP package^{58,59}. The projector-augmented wave scheme^{60,61} has been used to treat core electrons. Motivated by the fact that 2H and 3R bilayers have very similar lattice parameters⁶² and since upon geometry optimization on MoS₂ monolayers the obtained lattice parameter is 3.22 Å, we have kept this value for all the runs. No significant change in the interlayer distance, as defined here by the separation between the two parallel planes containing Mo atoms, is observed when passing from 2H to 3R configuration, i.e., 6.17 and 6.13 Å respectively. A grid of $15 \times 15 \times 1$ k-points has been used, in conjunction with a vacuum height of 21.9 Å,

for all the calculation cells. The geometry's optimization process has been performed at the PBE-D3 level³⁰ in order to include van der Waals interaction between layers. All the atoms were allowed to relax with a force convergence criterion below 0.005 eV/Å. Heyd-Scuseria-Ernzerhof (HSE) hybrid functional^{63–65} has been used as an approximation of the exchange-correlation electronic term, including SOC, to determine eigenvalues and wave functions as input for the full-frequency-dependent GW calculations⁶⁶ performed at the G_0W_0 level. An energy cutoff of 400 eV and a Gaussian smearing of 0.05 eV width have been chosen for partial occupancies, when a tight electronic minimization tolerance of 10^{-8} eV was set to determine with a good precision the corresponding derivative of the orbitals with respect to k needed in quasi-particle band structure calculations. The total number of states included in the GW procedure is set to 1280, in conjunction with an energy cutoff of 100 eV for the response function, after a careful check of the direct bandgap convergence (smaller than 0.1 eV as a function of k -points sampling). Band structures have been obtained after a Wannier interpolation procedure performed by the WANNIER90 program⁶⁷. All optical excitonic transitions have been calculated by solving the Bethe-Salpeter equation^{68,69}, using the 12 highest valence bands and the 16 lowest conduction bands to obtain eigenvalues and oscillator strengths on all systems. From these calculations, we report the absorbance values by using the imaginary part of the complex dielectric function.

Data availability

The data that support the findings of this study are available from the corresponding author upon request.

Received: 24 January 2020; Accepted: 6 April 2020;

Published online: 13 May 2020

References

- Novoselov, K. S., Mishchenko, A., Carvalho, A. & CastroNeto, A. H. 2D materials and van der Waals heterostructures. *Science* **353**, aac9439 (2016).
- Mak, K. F. & Shan, J. Photonics and optoelectronics of 2D semiconductor transition metal dichalcogenides. *Nat. Photonics* **10**, 216–226 (2016).
- Schaibley, J. R. et al. Valley depolarization dynamics and valley Hall effect of excitons in monolayer and bilayer MoS₂. *Nat. Rev. Mater.* **1**, 16055 (2016).
- Unuchek, D. et al. Room-temperature electrical control of exciton flux in a van der Waals heterostructure. *Nature* **560**, 340 (2018).
- Schneider, C., Glazov, M. M., Korn, T., Höfling, S. & Urbaszek, B. Two-dimensional semiconductors in the regime of strong light-matter coupling. *Nat. Commun.* **3**, 2695 (2018).
- Koperski, M. et al. Optical properties of atomically thin transition metal dichalcogenides: observations and puzzles. *Nanophotonics* **6**, 1289–1308 (2017).
- Dufferwiel, S. et al. Valley-addressable polaritons in atomically thin semiconductors. *Nat. Photonics* **11**, 497 (2017).
- Scuri, G. et al. Large excitonic reflectivity of monolayer MoSe₂ encapsulated in hexagonal boron nitride. *Phys. Rev. Lett.* **120**, 037402 (2018).
- Hong, X. et al. Ultrafast charge transfer in atomically thin MoS₂/WS₂ heterostructures. *Nat. Nanotechnol.* **9**, 682 (2014).
- Splendiani, A. et al. Emerging photoluminescence in monolayer MoS₂. *Nano Lett.* **10**, 1271 (2010).
- Mak, K. F., Lee, C., Hone, J., Shan, J. & Heinz, T. F. Atomically thin MoS₂: a new direct-gap semiconductor. *Phys. Rev. Lett.* **105**, 136805 (2010).
- Tonndorf, P. et al. Photoluminescence emission and Raman response of monolayer MoS₂, MoSe₂, and WSe₂. *Opt. Express* **21**, 4908–4916 (2013).
- Zhang, N. et al. Moire intralayer excitons in a MoSe₂/MoS₂ heterostructure. *Nano Lett.* **18**, 7651–7657 (2018).
- Tran, K. et al. Evidence for Moiré excitons in van der Waals heterostructures. *Nature* **567**, 71 (2019).
- Jin, C. et al. Observation of Moiré excitons in WSe₂/WS₂ heterostructure superlattices. *Nature* **567**, 76 (2019).
- Seyler, K. L. et al. Signatures of Moiré-trapped valley excitons in MoSe₂/WSe₂ heterobilayers. *Nature* **567**, 66 (2019).
- Alexeev, E. M. et al. Resonantly hybridized excitons in Moiré superlattices in van der Waals heterostructures. *Nature* **567**, 81 (2019).
- Cao, Y. et al. Unconventional superconductivity in magic-angle graphene superlattices. *Nature* **556**, 43 (2018).
- Wang, L. et al. Magic continuum in twisted bilayer WSe₂. Preprint at: <http://arxiv.org/abs/1910.12147> (2019).
- Shimazaki, Y. et al. Strongly correlated electrons and hybrid excitons in a moiré heterostructure. *Nature* **580**, 472–477 (2020).
- Weston, A. et al. Atomic reconstruction in twisted bilayers of transition metal dichalcogenides. Preprint at: <http://arxiv.org/abs/1911.12664> (2019).
- Sung, J. et al. Broken mirror symmetry in excitonic response of reconstructed domains in twisted MoSe₂/MoSe₂ bilayers. Preprint at: <http://arxiv.org/abs/2001.01157> (2020).
- Slobodeniuk, A. et al. Fine structure of k-excitons in multilayers of transition metal dichalcogenides. *2D Mater.* **6**, 025026 (2019).
- Gerber, I. C. et al. Interlayer excitons in bilayer MoS₂ with strong oscillator strength up to room temperature. *Phys. Rev. B* **99**, 035443 (2019).
- Deilmann, T. & Thygesen, K. S. Interlayer excitons with large optical amplitudes in layered van der Waals materials. *Nano Lett.* **18**, 2984–2989 (2018).
- Shree, S. et al. High optical quality of MoS₂ monolayers grown by chemical vapor deposition. *2D Mater.* **7**, 015011 (2019).
- Gong, Z. et al. Magnetolectric effects and valley-controlled spin quantum gates in transition metal dichalcogenide bilayers. *Nat. Commun.* **4**, 2053 (2013).
- Tong, Q. et al. Topological mosaics in Moiré superlattices of van der Waals heterobilayers. *Nat. Phys.* **13**, 356–362 (2016).
- Taniguchi, T. & Watanabe, K. Synthesis of high-purity boron nitride single crystals under high pressure by using Ba-BN solvent. *J. Cryst. Growth* **303**, 525–529 (2007).
- Grimme, S., Antony, J., Ehrlich, S. & Krieg, H. A consistent and accurate ab initio parametrization of density functional dispersion correction (DFT-D) for the 94 elements H–Pu. *J. Chem. Phys.* **132**, 154104 (2010).
- Xia, M. et al. Spectroscopic signatures of AA' and AB stacking of chemical vapor deposited bilayer MoS₂. *ACS Nano* **9**, 12246–12254 (2015).
- Jia, H. et al. Large-scale arrays of single- and few-layer MoS₂ nanomechanical resonators. *Nanoscale* **8**, 10677–10685 (2016).
- Mennel, L., Paur, M. & Mueller, T. Second harmonic generation in strained transition metal dichalcogenide monolayers: MoS₂, MoSe₂, WS₂, and WSe₂. *APL Photonics* **4**, 034404 (2019).
- Leisgang, N. et al. Optical second harmonic generation in encapsulated single-layer InSe. *AIP Adv.* **8**, 105120 (2018).
- George, A. et al. Controlled growth of transition metal dichalcogenide monolayers using Knudsen-type effusion cells for the precursors. *J. Phys. Mater.* **2**, 016001 (2019).
- Robert, C. et al. Optical spectroscopy of excited exciton states in MoS₂ monolayers in van der Waals heterostructures. *Phys. Rev. Mater.* **2**, 011001 (2018).
- Niehuus, I., Blob, A., Stiehm, T., de Vasconcellos, S. M. & Bratschitsch, R. Interlayer excitons in bilayer MoS₂ under uniaxial tensile strain. *Nanoscale* **11**, 12788–12792 (2019).
- Shinde, S. M. et al. Stacking-controllable interlayer coupling and symmetric configuration of multilayered MoS₂. *NPG Asia Mater.* **10**, e468 (2018).
- Huang, S. et al. Probing the interlayer coupling of twisted bilayer MoS₂ using photoluminescence spectroscopy. *Nano Lett.* **14**, 5500–5508 (2014).
- Yeh, P.-C. et al. Direct measurement of the tunable electronic structure of bilayer MoS₂ by interlayer twist. *Nano Lett.* **16**, 953–959 (2016).
- van Der Zande, A. M. et al. Tailoring the electronic structure in bilayer molybdenum disulfide via interlayer twist. *Nano Lett.* **14**, 3869–3875 (2014).
- Kormanyos, A. et al. k.p theory for two-dimensional transition metal dichalcogenide semiconductors. *2D Mater.* **2**, 022001 (2015).
- Castellanos-Gomez, A. et al. Deterministic transfer of two-dimensional materials by all-dry viscoelastic stamping. *2D Mater.* **1**, 011002 (2014).
- Kormányos, A., Zólyomi, V., Fal'ko, V. I. & Burkard, G. Tunable berry curvature and valley and spin Hall effect in bilayer MoS₂. *Phys. Rev. B* **98**, 035408 (2018).
- Horng, J. et al. Observation of interlayer excitons in MoSe₂ single crystals. *Phys. Rev. B* **97**, 241404 (2018).
- Wu, S. et al. Electrical tuning of valley magnetic moment through symmetry control in bilayer MoS₂. *Nat. Phys.* **9**, 149 (2013).
- Jones, A. M. et al. Spin-layer locking effects in optical orientation of exciton spin in bilayer WSe₂. *Nat. Phys.* **10**, 130–134 (2014).
- Clark, A. & Williams, R. The optical absorption properties of synthetic MoS₂. *J. Phys. D: Appl. Phys.* **1**, 1222 (1968).
- Roxlo, C., Chianelli, R., Deckman, H., Ruppert, A. & Wong, P. Bulk and surface optical absorption in molybdenum disulfide. *J. Vac. Sci. Technol. A* **5**, 555–557 (1987).
- Suzuki, R. et al. Valley-dependent spin polarization in bulk MoS₂ with broken inversion symmetry. *Nat. Nanotechnol.* **9**, 611 (2014).
- Latzke, D. W. et al. Electronic structure, spin-orbit coupling, and interlayer interaction in bulk MoS₂ and WS₂. *Phys. Rev. B* **91**, 235202 (2015).
- Du, L. et al. Temperature-driven evolution of critical points, interlayer coupling, and layer polarization in bilayer MoS₂. *Phys. Rev. B* **97**, 165410 (2018).
- Zhang, Y. et al. On valence-band splitting in layered MoS₂. *ACS Nano* **9**, 8514–8519 (2015).
- Jin, W. et al. Direct measurement of the thickness-dependent electronic band structure of MoS₂ using angle-resolved photoemission spectroscopy. *Phys. Rev. Lett.* **111**, 106801 (2013).

55. Arora, A. et al. Interlayer excitons in a bulk van der waals semiconductor. *Nat. Commun.* **8**, 639 (2017).
56. Arora, A. et al. Valley-contrasting optics of interlayer excitons in Mo- and W-based bulk transition metal dichalcogenides. *Nanoscale* **10**, 15571–15577 (2018).
57. Hsu, W.-T. et al., Tailoring excitonic states of van der Waals bilayers through stacking configuration, band alignment, and valley spin. *Science Advances* **5**, eaax7407 (2019).
58. Kresse, G. & Hafner, J. Ab initio molecular dynamics for liquid metals. *Phys. Rev. B* **47**, 558–561 (1993).
59. Kresse, G. & Furthmüller, J. Efficient iterative schemes for ab initio total-energy calculations using a plane-wave basis set. *Phys. Rev. B* **54**, 11169–11186 (1996).
60. Blöchl, P. E. Projector augmented-wave method. *Phys. Rev. B* **50**, 17953 (1994).
61. Kresse, G. & Joubert, D. From ultrasoft pseudopotentials to the projector augmented-wave method. *Phys. Rev. B* **59**, 1758–1775 (1999).
62. He, J., Hummer, K. & Franchini, C. Stacking effects on the electronic and optical properties of bilayer transition metal dichalcogenides MoS₂, MoSe₂, WS₂ and WSe₂. *Phys. Rev. B* **89**, 075409 (2014).
63. Heyd, J. & Scuseria, G. E. Assessment and validation of a screened Coulomb hybrid density functional. *J. Chem. Phys.* **120**, 7274 (2004).
64. Heyd, J., Peralta, J. E., Scuseria, G. E. & Martin, R. L. Energy band gaps and lattice parameters evaluated with the Heyd–Scuseria–Ernzerhof screened hybrid functional. *J. Chem. Phys.* **123**, 174101 (2005).
65. Paier, J. et al. Screened hybrid density functionals applied to solids. *J. Chem. Phys.* **124**, 154709 (2006).
66. Shishkin, M. & Kresse, G. Implementation and performance of the frequency-dependent GW method within the PAW framework. *Phys. Rev. B* **74**, 035101 (2006).
67. Mostofi, A. A. et al. wannier90: a tool for obtaining maximally-localised Wannier functions. *Comput. Phys. Commun.* **178**, 685–699 (2008).
68. Hanke, W. & Sham, L. J. Many-particle effects in the optical excitations of a semiconductor. *Phys. Rev. Lett.* **43**, 387 (1979).
69. Rohlfing, M. & Louie, S. G. Electron-hole excitations in semiconductors and insulators. *Phys. Rev. Lett.* **81**, 2312–2315 (1998).

Acknowledgements

Toulouse acknowledges funding from ANR 2D-vdW-Spin, ANR VallEx, ANR Magic-Valley, ITN 4PHOTON Marie Skłodowska Curie Grant Agreement No. 721394, and the Institut Universitaire de France. Growth of hexagonal boron nitride crystals was supported by the Elemental Strategy Initiative conducted by MEXT, Japan, and CREST (JPMJCR15F3), JST. I.C.G. thanks the CALMIP initiative for the generous allocation of computational times, through the project p0812, as well as the GENCI-CINES and GENCI-IDRIS for the grant A006096649. For FSU Jena, this project received funding from the joint European Union's Horizon 2020 and DFG research and innovation

programme FLAG-ERA under a Grant TU149/9-1, DFG Collaborative Research Center SFB 1375 NOA Project B2, and the Thüringer MWWDG via FGR 0088 2D-Sens. N.L. and R.J.W. acknowledge funding from the PhD School Quantum Computing and Quantum Technology, SNF (Project No. 200020_156637) and NCCR QSIT.

Author contributions

A.G. and A.T. grew the CVD samples. T.T. and K.W. grew the hBN bulk. I.P. and S.S. fabricated the encapsulated samples for optics and performed optical spectroscopy measurements. I.P., S.S., C.R., and X.M. analyzed the optical spectra. N.L., S.S., and R.J.W. performed SHG experiments. I.G. performed DFT-GW-BSE calculations. B.U. suggested the experiments and supervised the project. I.C.G. and B.U. wrote the manuscript with input from all the authors.

Competing interests

The authors declare no competing interests.

Additional information

Supplementary information is available for this paper at <https://doi.org/10.1038/s41467-020-16023-z>.

Correspondence and requests for materials should be addressed to I.C.G. or B.U.

Peer review information *Nature Communications* thanks Der-Yuh Lin, Steffen Michaelis de Vasconcellos, and the other, anonymous, reviewer(s) for their contribution to the peer review of this work.

Reprints and permission information is available at <http://www.nature.com/reprints>

Publisher's note Springer Nature remains neutral with regard to jurisdictional claims in published maps and institutional affiliations.



Open Access This article is licensed under a Creative Commons Attribution 4.0 International License, which permits use, sharing, adaptation, distribution and reproduction in any medium or format, as long as you give appropriate credit to the original author(s) and the source, provide a link to the Creative Commons license, and indicate if changes were made. The images or other third party material in this article are included in the article's Creative Commons license, unless indicated otherwise in a credit line to the material. If material is not included in the article's Creative Commons license and your intended use is not permitted by statutory regulation or exceeds the permitted use, you will need to obtain permission directly from the copyright holder. To view a copy of this license, visit <http://creativecommons.org/licenses/by/4.0/>.

© The Author(s) 2020